UNIVERSITY OF LEEDS

This is a repository copy of *Kinetic Study of Ni and NiO Reactions Pertinent to the Earth's Upper Atmosphere*.

White Rose Research Online URL for this paper:
http://eprints.whiterose.ac.uk/140154/

Version: Accepted Version

Article:
Mangan, TP, McAdam, N, Daly, SM orcid.org/0000-0001-7957-4514 et al. (1 more author) (2018) Kinetic Study of Ni and NiO Reactions Pertinent to the Earth's Upper Atmosphere. Journal of Physical Chemistry A, 123 (2). pp. 601-610. ISSN 1089-5639

https://doi.org/10.1021/acs.jpca.8b11382

Copyright © 2018 American Chemical Society. This document is the unedited Author's version of a Submitted Work that was subsequently accepted for publication in The Journal of Physical Chemistry, To access the final edited and published work see https://doi.org/10.1021/acs.jpca.8b11382.

Reuse
Items deposited in White Rose Research Online are protected by copyright, with all rights reserved unless indicated otherwise. They may be downloaded and/or printed for private study, or other acts as permitted by national copyright laws. The publisher or other rights holders may allow further reproduction and re-use of the full text version. This is indicated by the licence information on the White Rose Research Online record for the item.

Takedown
If you consider content in White Rose Research Online to be in breach of UK law, please notify us by emailing eprints@whiterose.ac.uk including the URL of the record and the reason for the withdrawal request.

White Rose university consortium
Universities of Leeds, Sheffield & York

eprints@whiterose.ac.uk
https://eprints.whiterose.ac.uk/

A Kinetic Study of Ni and NiO Reactions Pertinent to the Earth's Upper Atmosphere

Thomas P. Mangan, Nathanial McAdam, Shane M. Daly and John M. C. Plane*

School of Chemistry, University of Leeds, LS2 9JT, UK.

* corresponding author. Email: j.m.c.plane@leeds.ac.uk

Submitted to the Journal of Physical Chemistry A

November 2018

Abstract. Nickel atoms are injected into the Earth's mesosphere by meteoric ablation, producing a Ni layer between 70 and 105 km in altitude. The subsequent reactions of Ni and NiO with atmospherically relevant species were studied using the time-resolved pulsed laser photolysis-laser induced fluorescence technique, combined with electronic structure calculations and RRKM theory where appropriate. Results for bimolecular reactions (in cm^3 $molecule^{-1}$ s^{-1}): k(Ni + O_3, 293K) = (6.5 ± 0.7) $\times 10^{-10}$; k(NiO + O_3 → Ni + $2O_2$, 293 K) = (1.4 ± 0.5) × 10^{-10}; k(NiO + O_3 → NiO_2 + O_2, 293 K) = (2.5 ± 0.7) × 10^{-10}; k(NiO + CO, 190 - 377 K) = (3.2 ± 0.6) × 10^{-11} $(T/200)^{-0.19\pm0.05}$. For termolecular reactions (in cm^6 $molecule^{-2}$ s^{-1}, uncertainty $\pm\sigma$ over the stated temperature range): $\log_{10}(k_{rec,0}(Ni + O_2 + N_2, 190 - 455\ K)) = -37.592 + 7.168\log_{10}(T) - 1.5650(\log_{10}(T))^2$, σ=11%; $\log_{10}(k_{rec,0}(NiO + O_2 + N_2, 293 – 380\ K)) = -41.0913 + 10.1064\log_{10}(T) - 2.2610(\log_{10}(T))^2$, σ=22%; and $\log_{10}(k_{rec,0}(NiO + CO_2 + N_2, 191 – 375\ K)) = -41.4265 + 10.9640\log_{10}(T) - 2.5287(\log_{10}(T))^2$, σ =15%. The faster recombination reaction NiO + H_2O + N_2, which is clearly in the fall-off region over the experimental pressure range (3 – 10 Torr), is best described by: $\log_{10}(k_{rec,0}/cm^6\ molecule^{-2}\ s^{-1}) = -29.7651 + 5.2064\log_{10}(T) - 1.7118(\log_{10}(T))^2$, $k_{rec,\infty} = 6.0 \times 10^{-10} \exp(-171/T)\ cm^3\ molecule^{-1}\ s^{-1}$, broadening factor F_c = 0.84, σ=16%. The implications of these results in the atmosphere are then discussed.

1. Introduction

The Earth's atmosphere is subjected to a continuous influx of cosmic dust particles. The global input rate of this dust was recently estimated to be 43 ± 14 t d^{-1} (tonnes per day), of which 8 t d^{-1} ablates due to frictional heating of the particles as they collide with air molecules at hypothermal speeds.[1] Meteoric ablation is the major source of the layers of metal atoms that occur between 75 and 105 km, in a region of the atmosphere known as the mesosphere/lower thermosphere (MLT).[2] The layers of Na, K, Ca, Ca^+ and Fe have been studied in great detail over several decades by the ground-based lidar technique; and the Na, K, Mg and Mg^+ layers have also been observed by space-borne optical spectroscopy.[3] Recently, a Ni layer was observed for the first time by a lidar at the Poker Flat Research Range in Alaska (65° N), using the optical transition at 337.1 nm [Ni($z^3F_4^0$ – a^3F_4)].[4] Surprisingly, the Ni layer exhibited marked differences from other metals such as Fe, extending down to nearly 70 km and having a column density roughly 20 times larger than expected based on the elemental abundance of Ni in Carbonaceous Ivuna (CI) chondrites (1.1%).[5] Ni can be present in meteorites as a Fe-Ni alloy, but is present in the majority of chondrites as Fe-Ni sulphides.[6]

Understanding the chemistry that controls the metal layers in the MLT is important as they provide unique tracers of the chemistry and dynamics of a part of the atmosphere that can only be accessed directly by payloads on sub-orbital rockets. The metal atoms become oxidized in the mesosphere to form a range of oxides, hydroxides and carbonates which then aggregate into Meteoric Smoke Particles (MSPs).[3, 7] MSPs are thought to act as ice nuclei for polar mesospheric clouds[8] and condensation nuclei for sulphate aerosol that go on to form polar stratospheric clouds.[9] The composition and concentration of MSPs may influence these processes. To understand the characteristics of the newly-observed Ni layer and the likely Ni-containing molecules which will contribute to MSP formation, the gas-phase chemistry of Ni in the MLT needs to be understood.

Figure1 is a proposed reaction scheme for the likely neutral and ion reactions of Ni occurring in the MLT. This is based on our previous work on Fe and Mg,[3] and using electronic structure theory calculations of Ni species reacting with ambient MLT species to determine energetically viable reaction pathways (see Section 4 for further details). Note that the ion-molecule chemistry is included here for completeness, and is not the subject of the present study. The only relevant reaction that has, to our knowledge, been studied previously is the recombination of Ni with O_2 (at 295 K in an Ar bath gas).[10] The following reactions of Ni and NiO that were investigated in the present study (red arrows in Figure 1) are:

	ΔH^o(0 K)	
$Ni + O_2 (+ M) \rightarrow ONiO$	-259 kJ mol^{-1}	(R1)
$Ni + O_3 \rightarrow NiO + O_2$	-297 kJ mol^{-1}	(R2)
$NiO + O_3 \rightarrow Ni + 2O_2$	-3 kJ mol^{-1}	(R3a)
$\rightarrow ONiO + O_2$	-182 kJ mol^{-1}	(R3b)
$NiO + CO \rightarrow Ni + CO_2$	-136 kJ mol^{-1}	(R4)
$NiO + O_2 (+ M) \rightarrow ONiO_2$	-88 kJ mol^{-1}	(R5)
$NiO + H_2O (+ M) \rightarrow Ni(OH)_2$	-278 kJ mol^{-1}	(R6)
$NiO + CO_2 (+ M) \rightarrow NiCO_3$	-83 kJ mol^{-1}	(R7)

where M is a third body, and the standard reaction enthalpies (at 0 K) are calculated at the CBS-QB3 level of theory,[11, 12] apart from that for R1 which is taken from a recent multi-reference configuration interaction study.[13]

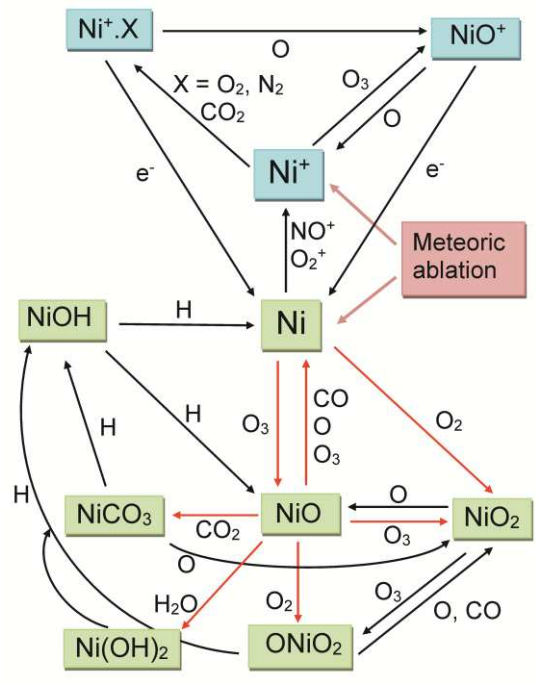

Figure 1. Proposed reaction scheme for the neutral and ion-molecule chemistry of Ni in the MLT, where meteoric ablation provides the initial source of Ni and Ni^+. Neutral and ionic species are shown in green and blue boxes, respectively. The kinetics of reactions indicated with red lines were measured in the present study.

2. Experimental

Reactions R1 – R7 were studied using the Pulsed Laser Photolysis-Laser Induced Fluorescence (PLP-LIF) technique. Figure 2 is a schematic diagram of the stainless steel reactor which has been used previously to study the kinetics of other mesospheric metal atoms and their oxides, including Si/SiO, Mg/MgO, Ca/CaO and Fe/FeO.[3]

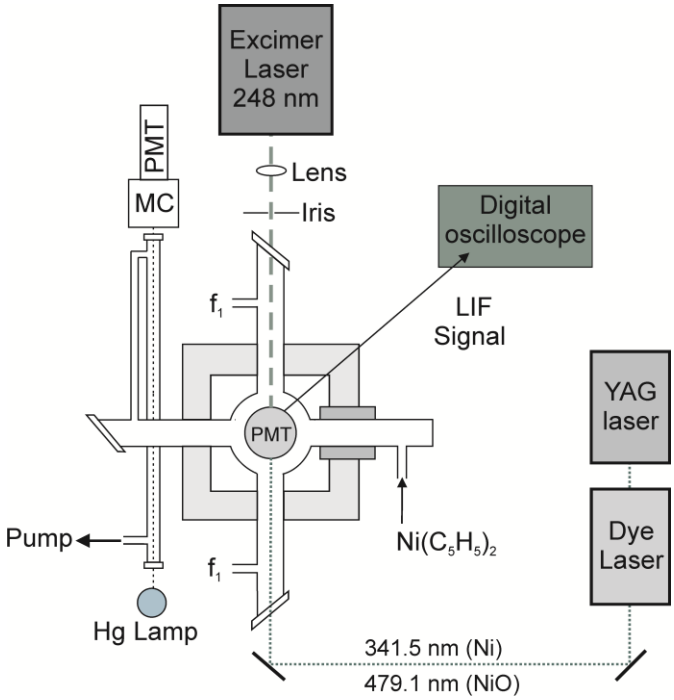

Figure 2. Schematic diagram of the PLP-LIF system for studying the kinetics of reactions of Ni and NiO. MC = monochromator; f_1 = reactant gas flow; PMT = photomultiplier tube.

The stainless steel reactor comprises a central chamber (volume = 400 cm^3) with four horizontal side arms that are mutually orthogonal, and one vertical side arm. The reaction chamber is surrounded by ceramic heaters housed within a stainless steel box, allowing for stable resistive heating up to 1100 K. Alternatively, the box can be filled with dry ice to reach a base temperature of 190 K. Reaction chamber temperatures were measured with a shielded thermocouple inserted directly into the centre of the reactor volume.

Ni atoms were generated in the reactor by the multiphoton dissociation of nickelocene (dicyclopentadienyl nickel, $[Ni(C_5H_5)_2]$) vapor at 248 nm using a KrF excimer laser (Lambda Physik COMPEX 102, typical pulse energy = 40 mJ, <5 mJ in the reactor (pulse rate = 10 Hz). The excimer beam was loosely focused to a point 15 cm beyond the centre of the reaction chamber using a lens (focal length = 50 cm). These experiments were limited to a maximum temperature of 450 K because there was clear evidence in experiments at higher temperatures that decomposition of the nickelocene precursor artificially increased reaction rates.

Ni atoms were probed either at 341.476 nm $[Ni(z^3F_4^0 – a^3D_3)]$ or at 339.105 nm $[Ni(z^3F_4^0 – a^3F_4)]$, using a frequency-doubled Nd:YAG pumped dye laser (Sirah CBR-G-30) with Pyridine 1 laser dye. The dye and excimer laser beams counter-propagated through opposing arms of the reactor (Figure 1). By varying the time delay between the dye laser (probe beam) and excimer laser (photolysis beam, t = 0), scans of the concentration of Ni/NiO with time were obtained. In a typical experiment each LIF signal time step was the average of 5 laser shots. The Ni LIF signal was collected through an interference filter (λ_{max} = 340 nm, FWHM = 10 nm) using a Photomultiplier Tube (PMT, Electron Tubes, model 9816QB) attached to the vertical side arm of the reactor, orthogonal to the laser beams. Loose focusing of the excimer laser to achieve multi-photon dissociation was necessary to produce Ni atoms. This also produced a population of Ni in excited states, the effect of which is discussed in Section 3. $NiO(X^3\Sigma^-)$ was probed at 479.108 nm[5] using Coumarin 102 dye, and monitored off resonance

using a cut-on filter at 495 nm. All the Ni and NiO transitions were calibrated using a wavelength meter (Bristol instruments 871) accurate to 0.8 pm.

Reactant gases (O_2, O_3, CO_2, CO, H_2O) were added via the PMT side arm and two laser beam side arms, mixing in the central chamber of the reactor. The flows in each experiment comprised the nickelocene vapor entrained in N_2 flow, the reactant flow and a balancing flow of the bath gas N_2 (total flow of 0.2 L/min). The reactant concentration was calculated using the calibrated mass flow rates and the pressure in the reactor, measured using a Baratron pressure gauge (MKS PR 4000). The total pressure in the system ranged between 3 and 10 Torr. The final arm of the reactor provides the exhaust outlet leading to an O_3 absorption cell and vacuum pump (Edwards E28).

O_3 was produced by corona discharge of O_2 in an ozoniser (Fischer OZ500) with a typical conversion efficiency of ~2%. The concentration of O_3 was monitored by absorption spectroscopy at 253.7 nm from a Hg Pen-ray lamp, using a 1m path length absorption cell downstream of the reactor and a monochromator (Minichrom, 300 μm slits) with a PMT (Hamamatsu Type H9306-13) (Figure 1). The O_3 concentration was then determined using the absorption cross section at 293 K of 1.16×10^{-17} cm^2 at 253.7 nm.[14]

Materials

N_2 (99.9999 % pure, Air Products), O_2 (99.999 %, pure Air Products), CO_2 (99.995 % pure, Air Products), and CO (99.5 % pure, Argo International) were used without any further purification. H_2O vapour was produced by freeze-pump thawing deionised water and subsequent dilution in a glass bulb on a glass vacuum gas-handling line. Nickelocene vapour (vapor pressure = 5 mTorr at 293 K [15]) was entrained within a flow of N_2 gas over a glass trap containing pure nickelocene crystals.

3. Results

3.1 Ni + O_2

The time-resolved LIF signals are described by a single exponential form $A \times \exp(-k' t)$, where the first-order decay coefficient k' is given by

$$k' = k_{diff} + k_1[O_2][M] \qquad (1)$$

k_{diff} is the rate of diffusion of Ni atoms out of the volume of the excimer laser that is within the line of sight of the PMT, and has a value < 800 s^{-1}. Figure 3 illustrates plots of the natural logarithm of the LIF signal against time. Note the increase in Ni(^{3}F) concentration within the first 100 μs of each kinetic trace, which is due to the quenching of electronically excited Ni atoms produced during photolysis of the nickelocene precursor. These excited atoms were quenched to the ground-state by the N_2 bath gas in ~ 100 μs,[16] and kinetic traces were therefore always fitted at longer times when there was no further evidence of highly excited metastable Ni atoms (i.e. above the low-lying Ni(^{3}D) state) playing a role.

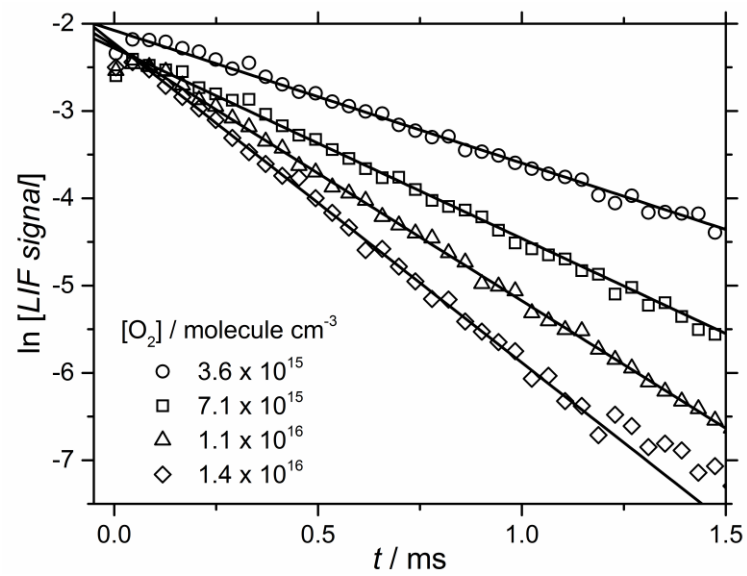

Figure 3. Kinetic decays of Ni(^{3}F) reacting with [O_2] (total pressure = 3 Torr). The lines are linear regression fits through each decay.

Figure 4 shows that plots of k' against [O_2] over the temperature range 191 – 455 K are linear with a slope providing the second-order rate coefficient at a particular pressure of N_2. The resulting third-order rate coefficients are plotted as function of temperature in Figure 5.

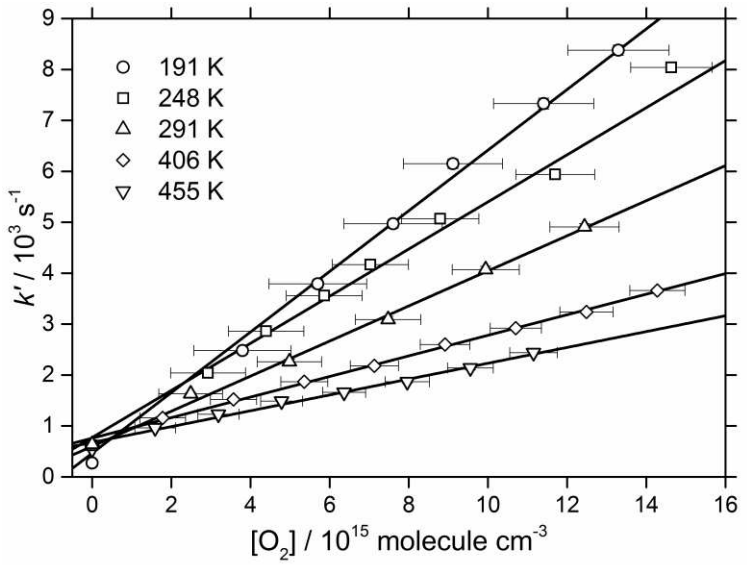

Figure 4. Plots of k' against [O_2] for R1 (3 Torr total pressure). The slopes of the linear regression fits yield the second-order rate coefficients, illustrating the negative temperature dependence of the reaction from 191 to 455 K.

Nickel has two low lying states, the ground state Ni(a^3F_4, configuration [Ar].$3d^8.4s^2$) and the excited Ni(a^3D_3, configuration [Ar].$3d^9.4s^1$) state which is only 204 cm^{-1} above the ground state so that the spin-orbit manifolds of these configurations overlap.[17] Note that the prefix in front of the atomic term symbol is conventionally used to distinguish terms of the same type and multiplicity from each other in complex atomic spectra.[18] In the present study most reactions

were investigated by probing the Ni(a^3D_3) excited state, as it produced significantly more LIF signal since the Einstein coefficient for the Ni($z^3F_4^0 – a^3D_3$) transition is 5.5×10^7 s^{-1}, compared with 1.8×10^7 s^{-1} for the Ni($z^3F_4^0 – a^3F_4$) transition.[17] As shown in Figure 5, R1 was studied at several temperatures between 190 and 410 K by using both Ni transitions, and the resulting rate coefficients agreed within error. This is likely to be because these states are rapidly thermally equilibrated on the time-scale of reaction. This is to be expected given their close separation in energy (the Boltzmann fraction of Ni in the a^3D_3 state varies from 14.3 to 26.5% between 191 and 400 K) and the relatively high pressure in the reactor (> 1 Torr N_2). Thus, the reaction kinetics of both states are tightly coupled, and either transition can be used as a spectroscopic marker for the overall kinetics which will be governed by the more reactive of the two states.

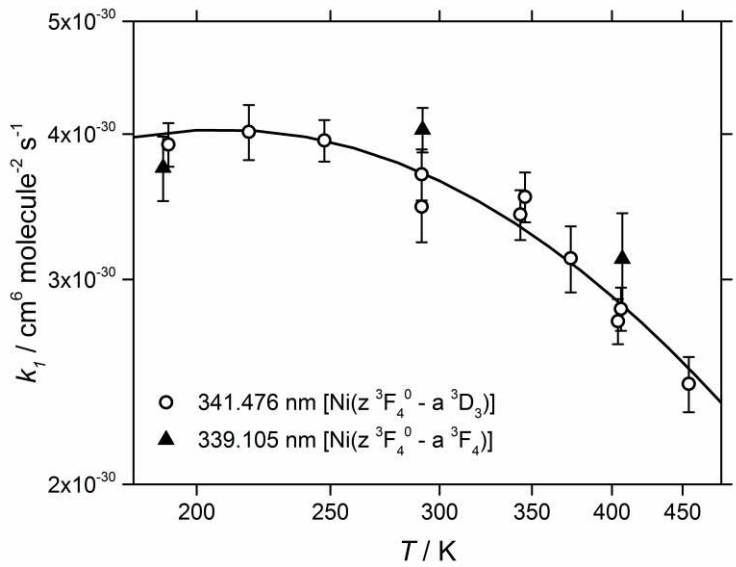

Figure 5. Third-order rate coefficient for R1 as a function of temperature where N_2 is the third body. Measurements were made using LIF transitions from the Ni (a^3F_4) ground state and the low-lying Ni(a^3D_3) excited state. The solid line is an RRKM fit to the experimental data.

3.2 Ni + O_3 → NiO + O_2

The loss of Ni in the presence of O_3 and O_2 should be described by:

$$k' = k_{diff} + k_2[O_3] + k_1[O_2] \qquad (2)$$

The points with square symbols in Figure 6 are a plot of k' as a function of [O_3]. This shows curvature at inceasing [O_3] (the dashed line is provided to guide the eye), which is caused by NiO being recycled back to Ni by reaction with O_3 (reaction R3a). The result is that the decay of Ni due to R2 is retarded, an effect that we have previously observed for reactions such as Na and Mg^+ with O_3.[19, 20] In order to prevent recycling of NiO back to Ni, HCl was added in large excess (by a factor of 25 over the maximum [O_3] i.e. 5×10^{14} molecules cm^{-3}). NiO reacts with HCl via channel R8a, which is effectively thermoneutral:

$$NiO + HCl \rightarrow NiCl + OH \qquad \Delta H^o = 1.6 \text{ kJ mol}^{-1} \qquad (R8a)$$

$$\rightarrow NiOH + Cl \qquad \Delta H^o = 78 \text{ kJ mol}^{-1} \qquad (R8b)$$

As shown in Figure 6, the decay rate of Ni is now significantly increased at the same [O_3]. The contribution of R1 (up to 12%) has been subtracted from k'. The linear regression fit in the

presence of HCl yields k_2(293 K) = (6.5 ± 0.7) × 10^{-10} cm^3 $molecule^{-1}$ s^{-1}. Kinetic decays recorded over a range of excimer pulse energies (nominal energy 30-70 mJ, maximum fluence in the reactor 6 × 10^{15} photons cm^{-2}) did not display a discernable change in the Ni first-order decay rate, suggesting that O_3 photolysis was not significant at the relatively low excimer fluence in the reactor. Indeed, as we show in Section 4, k_2 is very close to the long-range capture rate coefficient.

The large intercept of the plot in Figure 6 of 5100 s^{-1} is due to the reaction of Ni with HCl:

$$Ni + HCl \rightarrow NiCl + H \qquad \Delta H^o = -172 \text{ kJ mol}^{-1} \qquad \text{(R9)}$$

which therefore has a rate coefficient k_9(293 K) ~ 9 × 10^{-12} cm^3 $molecule^{-1}$ s^{-1}. There is a significant barrier on the PES for R9, calculated at the CBS-QB3 level of theory[12] to have a height of 23 kJ mol^{-1} (probably an overestimate by around 10 kJ mol^{-1} to be consistent with the magnitude of k_9).

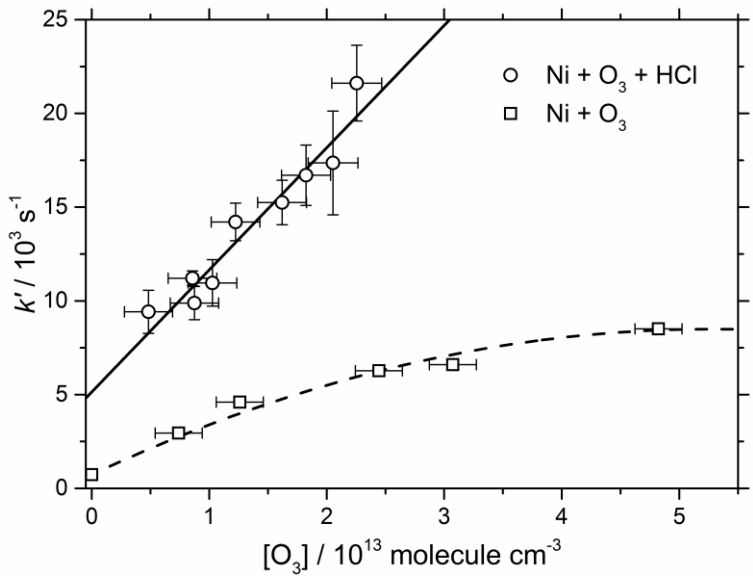

Figure 6. Plots of k' against [O_3] in the presence and absence of HCl at 293 K. The added HCl (5 × 10^{14} molecule cm^{-3}) reacts with NiO to prevent recycling back to Ni via reaction R3a.

3.3 Reactions of NiO

NiO + O_3

When studying reactions R3-R7, we were not aware of a direct photolytic source of NiO. Furthermore, when we explored using N_2O or NO_2 to produce NiO from Ni, both these oxidants were found to produce NiO too slowly to be useful for studying NiO kinetics (in agreement with a previous study of Ni + N_2O[16]). This meant that NiO had to be produced by reaction of Ni with O_3 via reaction R2. The resulting time-resolved behavior of NiO in the presence of O_3, O_2 and other reactants then had to be analysed through kinetic modeling.

The model comprised a set of differential equations accounting for the removal of Ni and NiO by O_2, O_3 and other reagents (reactions R4 - R7), as well as diffusional loss out of the volume created by the excimer laser and within the field-of-view of the PMT. This volume is essentially a cylinder of radius r = 0.6 cm. The diffusion coefficients of Ni, NiO and ONiO were calculated[21] from the dipole-induced dipole and long-range dispersion forces between the Ni

species and N_2, using the parameters in Table 1. The calculated diffusion rate of Ni out of the excimer laser volume, which is given by $5.81D/r^2$,[22] is in accord with the measured k_{diff} rates of 600 – 700 s^{-1} at 3 Torr. Ni has the largest diffusion coefficient because it does not have a dipole moment, and its polarizability is smaller than NiO and ONiO. In the model a $T^{1.83}$ dependence for the diffusion coefficients was assumed.[19, 21]

Table 1. Parameters and estimated diffusion coefficients for Ni species in N_2 at 293 K.

Species	Dipole moment Debye	Polarizability 10^{-24} cm^3	Ionization energy / eV	Diffusion coefficient[a] Torr cm^2 s^{-1}
Ni	-	6.8 [b]	7.64 [b]	128
NiO	4.43 ± 0.04 [c]	8.4 [d]	9.83 [d]	105
ONiO	-	11 [d]	8.82 [d]	100

[a] Calculated using the standard formalism in Maitland et al.[21]

[b] Handbook of Physics and Chemistry [23]

[c] Experimental value.[24]

[d] Calculated at the B3LYP/6-311+g(2d,p) level of theory.[11]

Reaction 3 was studied by measuring the time-resolved variation of the measured Ni and NiO LIF signals when Ni was produced in the presence of O_3 (and O_2, but without added HCl). The rate coefficients for both channels of R3, k_{3a} and k_{3b}, were included in the model as floating parameters. A non-linear least-squares fitting procedure was then used to scale and fit the model simulation to the experimental data after reaction times longer than 150 μs, when quenching of excited Ni states was complete (see above). The best-fit value for R3a ($NiO + O_3 \rightarrow Ni + 2O_2$) is $k_{3a}(293\ K) = (1.4 \pm 0.5) \times 10^{-10}$ cm^3 $molecule^{-1}$ s^{-1}, and R3b ($NiO + O_3 \rightarrow Ni + 2O_2$) is $k_{3b}(293\ K) = (2.5 \pm 0.7) \times 10^{-10}$ cm^3 $molecule^{-1}$ s^{-1}. The uncertainties were estimated using Monte Carlo sampling of the uncertainties of the kinetic parameters in the model, assuming a "top-hat" probability distribution, and repeating the fit to each experimental kinetic trace 10^3 times. The simulated fits to three experimental decays of Ni are shown in Figure 7, with the uncertainty envelope depicted by the dashed lines. The uncertainty mostly arises from uncertainties in $[O_3]$ and k_2. Note that the model satisfactorily captures the departure from single exponential decay behavior.

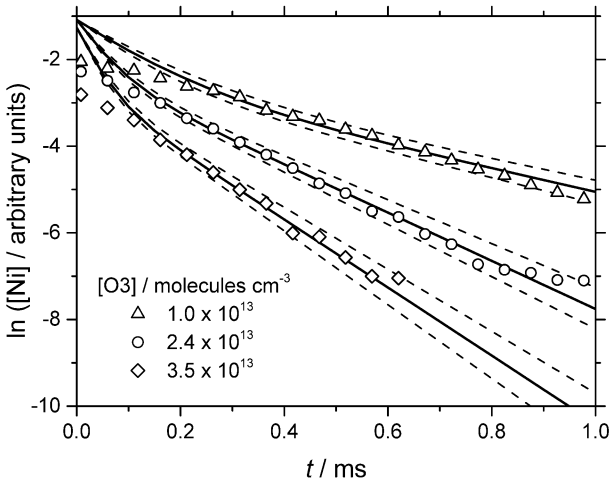

Figure 7. Time-resolved decays of the Ni concentration (in arbitrary units) in the presence of O_3 and O_2 at 295 K. The symbols are experimental values and the solid lines fitted simulations using the kinetic model. The dashed lines indicate the uncertainty envelope.

NiO + CO, O_2, H_2O and CO_2

The kinetic model, including the new rate coefficients for R3a and R3b, was then used to study R4 - R7 by fitting to time-resolved kinetic traces of NiO when Ni was produced in the presence of fixed [O_3] and varying concentrations of CO, O_2, H_2O or CO_2. Examples of fitted simulations to experimental data for R4 are shown in Figure 8. Background fits in the absence of the additional reactant (in this case CO) were first used to constrain the model [Ni] (taken before and after runs with CO added). The excellent fit in Figure 8 (top trace, [CO] = 0) demonstrates that the kinetic model with k_{3a} and k_{3b} optimised to fits of Ni decay profiles can equally well simulate the time-resolved NiO profile. Kinetic traces for experiments including CO, where k_4 is a floating parameter, were then fitted using the same least-squares method. As shown in the middle and lower traces in Figure 8, increasing [CO] decreases the NiO peak, while increasing the NiO tail at longer times, due to the recycling reaction NiO + CO → Ni + CO_2. Figure 9 illustrates the resulting variation of k_4 over the temperature range 190 – 376 K. A linear regression fit yields, $k_4(190 – 376\ K) = (3.2 \pm 0.6) \times 10^{-11} (T/200)^{-0.19\pm0.05}$ cm^3 $molecule^{-1}$ s^{-1} (uncertainty at the 95% confidence level).

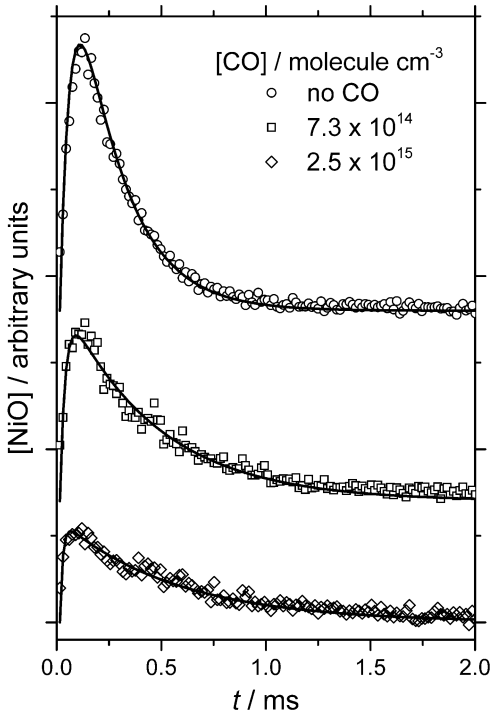

Figure 8. Time-resolved variation of the NiO concentration (in arbitrary units) in the presence of O_3 and varying CO (see figure legend). The solid lines are fitted model simulations to the experimental data (open symbols). Conditions: T = 295 K, P = 3 Torr, $[O_3] = 2 \times 10^{13}$ molecules cm^{-3}, $[O_2] = 1.2 \times 10^{15}$ molecule cm^{-3}. The data for each experiment is offset vertically for clarity.

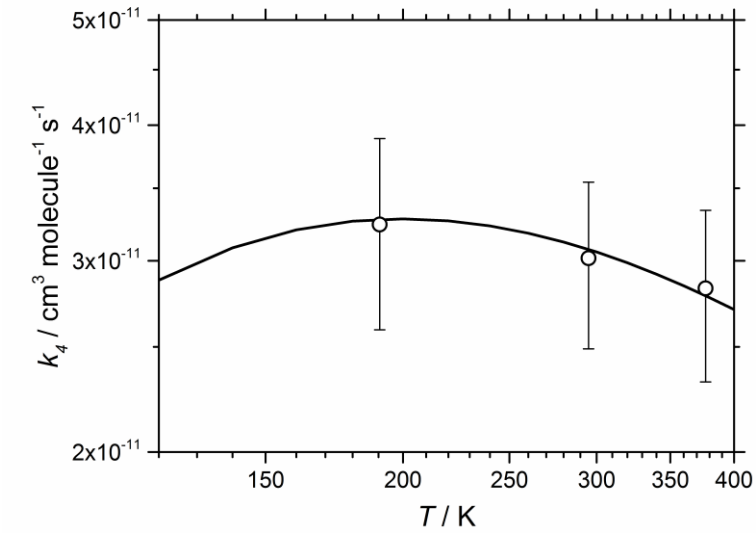

Figure 9. Rate coefficient for the reaction NiO + CO $\rightarrow$ Ni + CO_2 as a function of T. The solid line is a fit using RRKM theory.

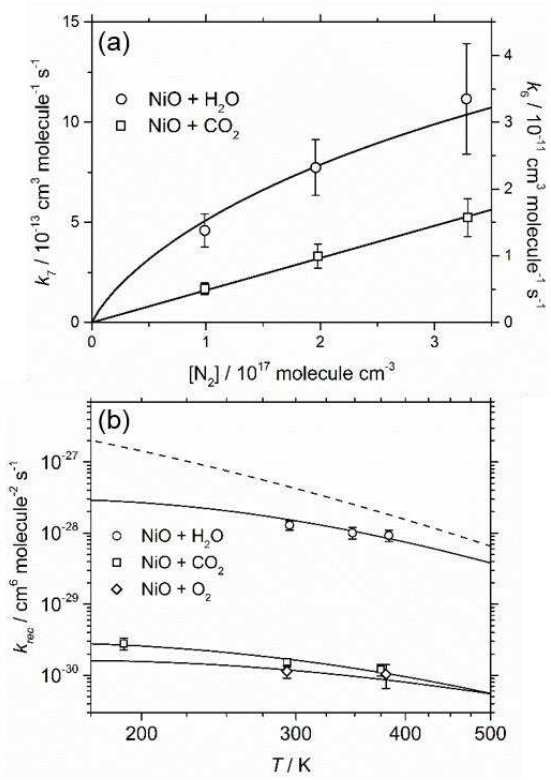

Figure 10. (a) Pressure dependence of R6 (NiO + H_2O, right-hand ordinate) and R7 (NiO + CO_2, left-hand ordinate) at 293 K. The symbols are experimental points, and the solid lines are RRKM fits. (b) Temperature dependence of R5, R6 and R7. The symbols are experimental values, and the solid lines are RRKM fits. Note that the R6 experimental points and RRKM fit are at a pressure of 3 Torr, and the dashed line shows the true low-pressure limiting rate coefficient for the reaction.

The recombination reactions R5-7 with N_2 as the third body were investigated using the same kinetic model to fit time-resolved traces of NiO. Reaction R5 (NiO + O_2) proved challenging to fit because O_2 also recombines with Ni (R1), so that varying [O_2] caused a comparatively small change in the time-resolved variation of Ni, which was only apparent above the signal-to-noise of the NiO LIF signal at temperatures between 293 and 380 K. Figure 10a shows the pressure dependence of the second-order rate coefficients for R6 and R7 at 293 K. Note that R6 is in the fall-off region over the pressure range 3 – 10 Torr. Figure 10b illustrates the negative temperature dependences of k_5, k_6 and k_7, with R6 proceeding ~100 times faster than R5 and R7. R5 and R7 are close to the low pressure limit in the experimental pressure range, yielding $k_5(293 - 380\ K) = (1.1 \pm 0.3) \times 10^{-30}\ (T/293)^{-0.4\pm0.1}$ and $k_7(191 - 375\ K) = (1.55 \pm 0.22) \times 10^{-30}\ (T/293)^{-1.28\pm0.34}$ $cm^6\ molecule^{-2}\ s^{-1}$ (quoted uncertainties at the 95% confidence level). A theoretical extrapolation of k_6 to the low-pressure limit is presented below.

4. Discussion

The individual second-order rate coefficients measured for R1 - R7 are listed as a function of temperature and pressure in Table S1 (in the Supporting Information, SI). In order to understand the unusual behaviour of several of these reactions, and also to extrapolate to the low pressure conditions of the MLT, electronic structure calculations were combined (where appropriate) with Rice-Ramsperger-Kassel-Markus (RRKM) theory. The hybrid density

functional B3LYP method was employed from within the Gaussian 16 suite of programs,[11] combined with the 6-311+G(2d,p) triple-ζ basis set. Molecular geometries were first optimized and checked for wave function stability, and their respective vibrational frequencies were calculated. More accurate energies were then determined using the Complete Basis Set (CBS-QB3) method of Petersson and co-workers.[12] The resulting geometries, rotational constants, vibrational frequencies and heats of formation of NiO, $ONiO_2$, $NiCO_3$ and $Ni(OH)_2$ are listed in Table S2 in the SI, and the geometries of these molecules are illustrated in Figure S1. Table S2 also contains relevant data for the stationary points on the NiO + CO and Ni + O_2 reaction potential energy surfaces (PES).

RRKM theory is used to calculate the pressure-dependent recombination rate coefficient between the low- and high-pressure limiting rate coefficients i.e. $k_{rec,0}$ and $k_{rec,\infty}$, respectively. Here we use a solution of the Master Equation (ME) based on the inverse Laplace transform method.[25] We have applied this formalism previously to reactions of metal-containing species where stable intermediates are present on the PES,[26, 27] and so only a brief description is given here. These reactions proceed via the formation of an excited adduct, which can either dissociate back to reactants or forward to products, or be stabilized into one or more energy wells by collision with a third body. The internal energy of the adduct is divided into a contiguous set of grains (width typically 30 – 70 cm^{-1}), each containing a bundle of rovibrational states. Each grain is then assigned a set of microcanonical rate coefficients for dissociation back to the reactants, and to products (if appropriate). These rate coefficients are determined using inverse Laplace transformation to link them directly to $k_{rec,\infty}$. For these neutral reactions, $k_{rec,\infty}$ should be close to the typical capture rate coefficient with a small positive temperature dependence characteristic of a long-range potential governed by the dispersion and dipole-induced dipole force (the measured dipole moment of NiO is 4.43 ± 0.04 D [24]). The density of states of the adduct is calculated using the Beyer–Swinehart algorithm[28] for the vibrational modes (without making a correction for anharmonicity) and a classical densities of states treatment for the rotational modes (the vibrational frequencies and rotational constants are listed in Table S2 of the SI). The probability of collisional transfer between grains was estimated using the exponential down model, where the average energy for downward transitions $\langle \Delta E \rangle_{down}$ was set to between 200 and 300 cm^{-1} which is typical of M = N_2 at 300 K, with a T^{α} temperature dependence where α is a small number between -1 and 1.[28] The ME, which describes the evolution with time of the grain populations of the adduct, is expressed in matrix form and then solved to yield the rate coefficients to form stable intermediates or products, at a specified pressure and temperature.

4.1 Ni + O_3 and NiO + O_3

R2 is fast with k_2(293 K) = (6.5 ± 0.7) × 10^{-10} cm^3 $molecule^{-1}$ s^{-1}. The ionization energy of Ni is too large (7.64 eV [23]) for a simple electron jump mechanism[29] to operate, since the avoided crossing between the ionic and covalent surfaces would be at only 2.6 Å with a rate coefficient of 1.0 × 10^{-10} cm^3 $molecule^{-1}$ s^{-1}. Instead, the rate coefficient can be compared with long-range capture theory, where the reaction is controlled by the dipole-induced dipole and dispersion forces. Using the data for Ni in Table 1, and a polarizability for O_3 of 3.21 × 10^{-24} cm^3 and ionization potential of 12.43 eV,[23] the ion-induced dipole capture rate is 1.1 × 10^{-10} cm^3 $molecule^{-1}$ s^{-1}, and that due to the dispersion force is 4.8 × 10^{-10} cm^3 $molecule^{-1}$ s^{-1}. Following the recommendation of Georgievskii and Klippenstein,[30] a good estimate of the overall capture rate is given by 1.3 times the larger of these terms. This gives 6.2 × 10^{-10} cm^3 $molecule^{-1}$ s^{-1}, which is in good agreement with the measured k_2, and provides further evidence that O_3 photolysis was not significant in the experiment. A small $T^{1/6}$ dependence for k_2 is then expected.[30]

In the case of R3, the overall rate coefficient $k_{3a} + k_{3b} = (3.9 \pm 0.9) \times 10^{-10}$ cm^3 molecule^{-1} s^{-1}, which is 60% of the capture rate coefficient estimated in the same way as for R2. The branching ratio to form Ni is 36%.

4.2 Ni + O_2 + N_2

The previous measurement of k_1 with M = Ar was $(1.7 \pm 0.3) \times 10^{-30}$ cm^6 molecules^{-2} s^{-1} at 296 K.[10] This is slower by a factor of 0.46 ± 0.15 than the result of the present study, which may be explained by the relative efficiencies of Ar and N_2 as third bodies.[28] As shown in Figure 5, the rate coefficient for R1 increases with decreasing T down to around 210 K, and then plateaus and starts to decrease slightly. The PES for this reaction is shown in Figure 11(a), based on the recent high level theory study.[13] The reaction produces the triangular NiO_2 initially (Figure S1 in the SI); an asymmetric Ni-O_2 with a Ni-O-O bond angle of 123.5^o is about 80 kJ mol^{-1} less stable, and linear Ni-O-O is not stable. The Ni can then insert into the O_2 to form the much more stable linear ONiO. Reaction to ONiO is therefore favoured by the much higher density of rovibrational states, but only if the low barrier between these two isomers (3.7 kJ mol^{-1} with respect to the reactants) can be cleared. At the lowest experimental pressure of 3 Torr, the reaction largely produces NiO_2 at very low temperatures, and ONiO at higher temperatures: for example, 54% of the product is NiO_2 at 100 K, but this decreases to only 1.8% at 600 K. The product ratio is somewhat pressure dependent: at a pressure of 0.003 Torr which is typical of 85 km in the atmosphere, 35% of the product is NiO_2 at 100 K, and 1.6% at 600 K. Note that both triangular NiO_2 and ONiO (but not linear or asymmetric Ni-O_2) have been observed in matrix isolation studies, with relative yields depending on the nature of the matrix.[13] The RRKM fit through the data is shown by the solid line in Figure 5, using the optimized parameters listed in Table S3 in the SI. The fitted temperature dependence is then: $\log_{10}(k_5(T)/\text{cm}^6\ \text{molecule}^{-2}\ \text{s}^{-1}) = -37.592 + 7.168\log_{10}(T) - 1.5650(\log_{10}(T))^2$, with an uncertainty of ±11% within the experimental temperature range (191 – 455 K).

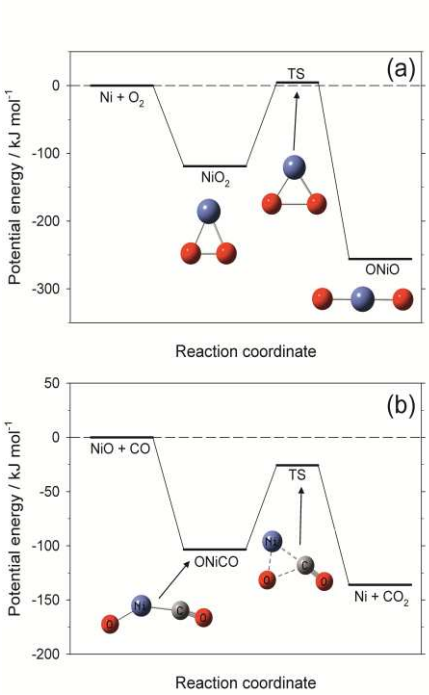

Figure 11. (a). Potential energy surface for the Ni + O_2 reaction forming NiO_2 and ONiO. Energies from Hübner and Himmel.[13] (b) Potential energy surface for the NiO + CO → Ni + CO_2 reaction. Calculated at the CBS-QB3 level of theory. Atom colors: oxygen (red); carbon (grey); nickel (blue)

4.3 NiO + CO

As shown in Figure 9, k_4 is around 3×10^{-11} cm^3 molecule^{-1} s^{-1}, with a possibly slightly negative T-dependence. This result can be compared with three other metal oxide + CO reactions for which kinetic data is available: k(NaO + CO, 296 K) = $(2.1 \pm 0.5) \times 10^{-10}$ cm^3 molecule^{-1} s^{-1} [31]; k(MgO + CO, 295 K) = $(1.1 \pm 0.3) \times 10^{-11}$ cm^3 molecule^{-1} s^{-1};[32] and k(FeO + CO, 295 K) = 1.5×10^{-13} cm^3 molecule^{-1} s^{-1}, obtained by extrapolating the expression derived by Smirnov[33] from detailed balance with high temperature (1180 - 2380 K) shock tube measurements of the reverse reaction Fe + $CO_2 \rightarrow$ FeO + CO. Thus, while being within a factor of 3 and 7 of the MgO and NaO + CO reactions, respectively, the NiO reaction is ~200 times faster than the FeO reaction. A likely reason for this is discussed below.

Figure 11(b) illustrates the PES for NiO + CO. The reaction involves forming a fairly stable OC-NiO intermediate that is bound by 104 kJ mol^{-1}. However, this can promptly dissociate over a barrier to the Ni + CO_2 products, since the barrier is submerged by 26 kJ mol^{-1} with respect to the reactants. The RRKM fit to this reaction (parameters in Table S3) is shown in Figure 9. The very slight temperature dependence is captured well, with k_4 increasing slightly between 400 and 200 K, and then decreasing slowly at lower temperatures. The barrier on the PES is far enough below the surface that an insignificant fraction (8×10^{-8} at 295 K and 10 Torr) of the OC-NiO complex forms compared to the Ni + CO_2 product. Nevertheless, because of the relatively large uncertainty in the experimental data, we recommend a simple linear fit through the three data points: $k_4(T) = (3.2 \pm 0.6) \times 10^{-11} (T/200)^{-0.19\pm0.05}$ cm^3 molecule^{-1} s^{-1}, which agrees within 20% with the RRKM fit between 120 and 400 K.

In contrast to R4, FeO + CO has a barrier that is calculated at the CBS-QB3 level to be 21.6 kJ mol^{-1} above the reactants, which explains why the reaction is so much slower.

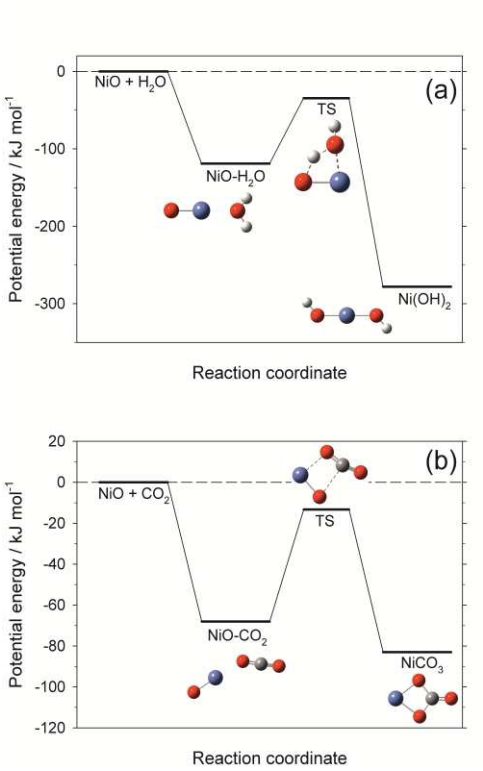

Figure 12. (a) The potential energy surface for the recombination of NiO and H_2O. (b) The potential energy surface for the recombination of NiO and CO_2. Calculated at the CBS-QB3 level of theory. Atom colors: oxygen (red); hydrogen (white); carbon (grey); nickel (blue).

4.4 NiO + O_2, H_2O and CO_2

Figure 10(a) shows that R6 (NiO + H_2O) is already in the fall-off region over the experimental pressure range, and so an RRKM extrapolation to the low pressures that characterise the MLT is essential. The reaction PES is illustrated in Figure 12(a). NiO forms a fairly strongly-bound ONi-H_2O adduct, which then rearranges over a submerged barrier to form the di-hydroxide, $Ni(OH)_2$. Since the overall reaction is strongly exothermic ($\Delta H^o(0\ K) = -278$ kJ mol^{-1}), the reaction is comparatively fast and hence in the fall-off region at 1 Torr of N_2. The RRKM fit is shown with a solid line in Figure 10(a) (see Table S3 for the optimized RRKM parameters). Figure 10(b) shows the measured temperature dependence of k_6 at 3 Torr, which compares well with the RRKM fit. The dashed line illustrates the low-pressure limiting rate coefficient, k_{6rec0}, which significantly larger (e.g. by a factor of 3 at 300 K), as expected. The rate coefficient can then be expressed by a Lindemann expression modified by a broadening factor F_c:[34] $\log_{10}(k_{6rec,0}$ / cm^6 molecule^{-2} s^{-1}) = -29.7651 + 5.2064$\log_{10}$(T) - 1.7118($\log_{10}$(T))^2; $k_{6rec,\infty} = 6.0 \times 10^{-10}$ exp(-171/T) cm^3 molecule^{-1} s^{-1}; $F_c = 0.84$, with an uncertainty of ±16% within the experimental temperature range (191 – 375 K).

The PES for reaction R7 is illustrated in Figure 12(b). This shows that the reaction involves first forming an ONi-OCO adduct, which rearranges over a submerged barrier to form $NiCO_3$. Although the overall reaction is not particularly exothermic ($\Delta H^o(0\ K) = -83$ kJ mol^{-1}), the large number of low vibrational frequencies in the carbonate product (Table S2) ensures that the rate coefficient is reasonably large. The ONi-OCO adduct is only bound by 67 kJ mol^{-1}, and so the two lowest frequencies (35 and 121 cm^{-1}) were treated as a 2-dimensional hindered rotor, with a barrier $V_0 = 14$ kJ mol^{-1} (see Table S3 for the other fitted RRKM parameters). The pressure- and temperature-dependent RRKM fits to the experimental data-points are shown in Figure 10, yielding $\log_{10}(k_7$ / cm^6 molecule^{-2} s^{-1}) = -41.4265 + 10.9640$\log_{10}$(T) - 2.5287($\log_{10}$(T))^2, with an uncertainty of ±15% within the experimental temperature range (191 – 375 K).

Reaction 5 involves simple addition of O_2 to NiO to form the most stable isomer, which is $ONiO_2$ (Figure S1) with triplet spin multiplicity ($\Delta H^o(0\ K) = -145$ kJ mol^{-1}). Singlet and quintet $ONiO_2$ are less stable than the triplet by 51 and 57 kJ mol^{-1}, respectively. The most stable ozonide NiO_3 isomer is the triplet, which is 124 kJ mol^{-1} less stable than the triplet $ONiO_2$ isomer. The RRKM fit (Figure 10b; fitted parameters in Table S3), yields $\log_{10}(k_5$(T) / cm^6 molecule^{-2} s^{-1}) = -41.0913 + 10.1064$\log_{10}$(T) - 2.2610($\log_{10}$(T))^2 with an uncertainty of ±22% within the experimental temperature range (293 – 380 K).

In comparison with the analogous FeO reactions at room temperature,[35] the NiO reactions with H_2O and CO_2 are faster by factors of 1.5 and 5, respectively, whereas the O_2 recombination is 3 times slower.

4.5 Atmospheric implications

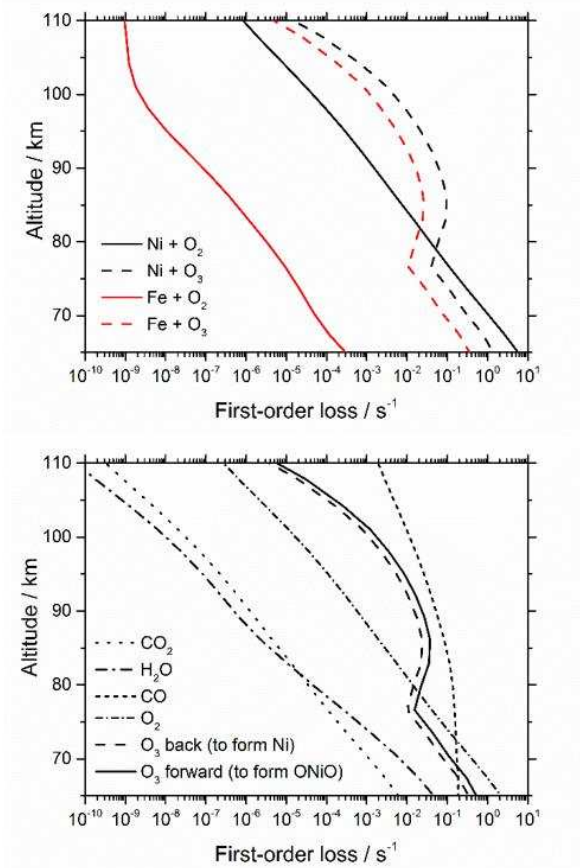

Figure 13. First-order removal rates in the MLT between 65 and 110 km, at midday during January at 40°N. Top panel: removal rates of Ni and Fe through reaction with O_3 and O_2, where the Fe rate coefficients are from a recent review.[36] Bottom panel: removal rates of NiO.

In order to ascertain the relative importance in the MLT of reactions R1 – R7, the rate coefficients were combined with profiles of the relevant reactant species, temperature and pressure. The profiles of these parameters between 65 and 110 km were taken from the Whole Atmosphere Community Climate Model (WACCM).[37] Figure 13 shows the first-order loss rates of Ni and NiO as a function of height. The top panel compares the Ni and Fe loss rates. In contrast to Fe, the Ni + O_2 loss pathway becomes competitive with the Ni + O_3 pathway around 80 km, which is below the 87 km peak of the Ni layer.[4] This difference is due to the ~1000 times faster reaction of Ni with O_2 compared to Fe[38] under these conditions. Note that O_3 increases in the MLT by around 1 order of magnitude at night,[3] when the formation rates of NiO and ONiO would be essentially the same.

Inspection of the bottom panel of Figure 13 shows that the recycling reaction of NiO with CO dominates, due to the relatively fast k_4 and the presence of significant CO in the MLT (formed primarily by CO_2 photolysis). The O_3 reaction recycling NiO back to Ni is also significant. In the future we plan to investigate the reaction NiO + O which, by analogy with the other meteoric metals,[3] may also make a major contribution to NiO recycling.

In terms of the recombination reactions, R5 (NiO + O_2) is the most competitive because of the high concentration of O_2. Although k_6 is around 2 orders of magnitude faster (Figure 10(b)), the low concentration of H_2O (just a few ppm) means that R6 is the least important recombination reaction above 80 km. However, given that $Ni(OH)_2$ is so much more stable

than $ONiO_2$ or $NiCO_3$, it is likely to be the major Ni reservoir, formed from $ONiO_2$ and $NiCO_3$ through these exothermic reactions:

$$ONiO_2 + H_2O \rightarrow Ni(OH)_2 + O_2 \qquad \Delta H = -133 \text{ kJ mol}^{-1} \qquad \text{(R10)}$$

$$NiCO_3 + H_2O \rightarrow Ni(OH)_2 + CO_2 \qquad \Delta H = -195 \text{ kJ mol}^{-1} \qquad \text{(R11)}$$

The potential energy surfaces for R10 and R11 are shown in Figure S2 (SI). In both cases, an initial complex with H_2O forms which then dissociates over a submerged barrier to $Ni(OH)_2$.

5. Conclusions

The reactions of Ni and NiO with atmospherically relevant species have been experimentally investigated using the PLP-LIF technique, all but one of them (R1) for the first time. The reaction kinetics are then explained using electronic structure theory combined with RRKM calculations. Reactions R1 and R4 exhibit unusual temperature dependences, which are explained by shallow submerged barriers on their potential energy surfaces. Theoretical fits to the experimental data were then used to extrapolate to the temperatures (120 – 240 K) and pressures (< 5 Pa) of the MLT region. A summary of the rate coefficients is given in Table 2.

Table 2. Summary of reaction rate coefficients measured in the present study.

No.	Reaction	Rate coefficient [a]
R1	$Ni + O_2 (+N_2) \rightarrow NiO_2$	$k_{rec,0} = 10^{-37.592 + 7.168 log_{10}(T) - 1.5650 (log_{10}(T))^2}$
R2	$Ni + O_3 \rightarrow NiO + O_2$	$(6.5 \pm 0.7) \times 10^{-10} (T/293)^{1/2}$
R3a	$NiO + O_3 \rightarrow Ni + 2O_2$	$(1.4 \pm 0.5) \times 10^{-10} (T/293)^{1/2}$
R3b	$NiO + O_3 \rightarrow NiO_2 + O_2$	$(2.5 \pm 0.7) \times 10^{-10} (T/293)^{1/2}$
R4	$NiO + CO \rightarrow Ni + CO_2$	$(3.2 \pm 0.6) \times 10^{-11} (T/200)^{-0.19 \pm 0.05}$
R5	$NiO + O_2 (+N_2) \rightarrow ONiO_2$	$k_{rec,0} = 10^{-41.0913 + 10.1064 log_{10}(T) - 2.2610 (log_{10}(T))^2}$
R6	$NiO + H_2O (+N_2) \rightarrow Ni(OH)_2$	$k_{rec,0} = 10^{-29.7651 + 5.2064 log_{10}(T) - 1.7118 (log_{10}(T))^2}$
		$k_{rec,\infty} = 6.0 \times 10^{-10} \exp(-171/T)$ [b]; $F_c = 0.84$
R7	$NiO + CO_2 (+N_2) \rightarrow NiCO_3$	$k_{rec,0} = 10^{-41.4265 + 10.9640 log_{10}(T) - 2.25287 (log_{10}(T))^2}$

[a] Units for termolecular reactions: cm^6 $molecule^{-2}$ s^{-1} (see Section 4 for uncertainties). Units for bimolecular reactions: cm^3 $molecule^{-1}$ s^{-1}.

In the MLT, Ni reacts most rapidly with O_3 above 80 km, and at a similar rate with O_2 below 80 km. Interestingly, the NiO + CO reaction rapidly recycles NiO to Ni, which may explain the unexpected observation of a significant concentration of Ni atoms below 80 km, unlike other metals such as Fe.[4]

Supporting Information. Contains the following: Table S1 listing second-order rate coefficients as a function of temperature and pressure; Table S2 listing the molecular properties and heats of formation of Ni-containing molecules; Table S3 of parameters used in the RRKM

fits to reaction kinetics; Figure S1 illustrating the geometries of Ni-containing molecules; and Figure S2 showing the potential energy surfaces for R10 and R11.

Acknowledgements

This work was supported by the UK Natural Environment Research Council (grant number NE/P001815/1). SMD has a research studentship funded by the NERC SPHERES doctoral training programme. We thank Dr Mark Blitz (University of Leeds) and Dr Juan Carlos Gómez Martín (Instituto de Astrofísica de Andalucía) for advice on the experimental design, and Natasha Aylett (University of Leeds) for supplying WACCM output. All the second-order rate coefficients, and the ab initio geometries, rotational constants, vibrational frequencies and heats of formation for the relevant Ni-containing molecules are listed in the Supplementary Information.

References

1. Carrillo-Sánchez, J. D.; Nesvorný, D.; Pokorný, P.; Janches, D.; Plane, J. M. C. Sources of Cosmic Dust in the Earth's Atmosphere. Geophys. Res. Lett. **2016,** 43, 11979-11986.

2. Plane, J. M. C. Atmospheric Chemistry of Meteoric Metals. Chem. Rev. **2003,** 103, 4963-4984.

3. Plane, J. M. C.; Feng, W.; Dawkins, E. C. M. The Mesosphere and Metals: Chemistry and Changes. Chem. Rev. **2015,** 115, 4497-4541.

4. Collins, R. L.; Li, J.; Martus, C. M. First Lidar Observation of the Mesospheric Nickel Layer. Geophys. Res. Lett. **2015,** 42, 665-671.

5. Balfour, W. J.; Cao, J.; Jensen, R. H.; Li, R. The Spectrum of Nickel Monoxide between 410 and 510 nm: Laser-induced Fluorescence and Dispersed Fluorescence Measurements. Chem. Phys. Lett. **2004,** 385, 239-243.

6. Berger, E. L.; Lauretta, D. S.; Zega, T. J.; Keller, L. P. Heterogeneous Histories of Ni-bearing Pyrrhotite and Pentlandite Grains in the CI Chondrites Orgueil and Alais. Meteor. Planet. Sci. **2016,** 51, 1813-1829.

7. Kalashnikova, O.; Horanyi, M.; Thomas, G. E.; Toon, O. B. Meteoric Smoke Production in the Atmosphere. Geophys. Res. Lett. **2000,** 27, 3293-3296.

8. Rapp, M.; Thomas, G. E. Modeling the Microphysics of Mesospheric Ice Particles: Assessment of Current Capabilities and Basic Sensitivities. J. Atmos. Solar-Terr. Phys. **2006,** 68, 715-744.

9. James, A. D.; Brooke, J. S. A.; Mangan, T. P.; Whale, T. F.; Plane, J. M. C.; Murray, B. J. Nucleation of Nitric Acid Hydrates in Polar Stratospheric Clouds by Meteoric Material. Atmos. Chem. Phys. **2018,** 18, 4519–4531.

10. Brown, C. E.; Mitchell, S. A.; Hackett, P. A. Dioxygen Complexes of 3d Transition-metal atoms: Formation Reactions in the Gas Phase. J. Phys. Chem. **1991,** 95, 1062-1066.

11. Frisch, M. J.; Trucks, G. W.; Schlegel, H. B.; Scuseria, G. E.; Robb, M. A.; Cheeseman, J. R.; Scalmani, G.; Barone, V.; Petersson, G. A.; Nakatsuji, H., et al. Gaussian 16, Revision B.01, Gaussian, Inc.: Wallingford, CT, USA, 2016.

12. Montgomery, J. A.; Frisch, M. J.; Ochterski, J. W.; Petersson, G. A. A Complete Basis Set Model Chemistry. VII. Use of the Minimum Population Localization Method. J. Chem. Phys. **2000,** 112, 6532-6542.

13. Hübner, O.; Himmel, H. J. Cyclic and Linear NiO_2: A Multireference Configuration Interaction Study. J. Phys. Chem. A **2012,** 116, 9181-9188.

14. Molina, L. T.; Molina, M. J. Absolute Absorption Cross Sections of Ozone in the 185 to 350 nm Wavelength Range. J. Geophys. Res. - Atmos. **1986,** 91, 14501-14508.

15. Brown, C. E.; Blitz, M. A.; Decker, S. A.; Mitchell, S. A. Multiphoton Dissociation of Nickelocene for Kinetic Studies of Nickel Atoms. In Laser Chemistry of Organometallics, American Chemical Society: 1993; Vol. 530, pp 177-187.

16. Campbell, M. L.; Kölsch, E. J.; Hooper, K. L. Kinetic Study of the Reactions of Gas-Phase V($a^4F_{3/2}$), Cr (a^7S_3), Co ($a^4F_{9/2}$), Ni (a^3F_4, a^3D_3) and Zn ($4s^2\ ^1S_0$) Atoms with Nitrous Oxide. J. Phys. Chem. A **2000,** 104, 11147-11153.

17. Kramida, A.; Ralchenko, Y.; Reader, J.; Team, N. A., NIST Atomic Spectra Database (version 5.6.1), https://physics.nist.gov/asd. National Institute of Standards and Technology: Gaithersburg, MD, 2018.

18. Moore, C. E. Atomic Energy Levels, Volume 2. National Bureau of Standards: Washington, D. C., 1952.

19. Helmer, M.; Plane, J. M. C. A Study of the Reaction NaO_2+ O → NaO+ O_2: Implications for the Chemistry of Sodium in the Upper Atmosphere. J. Geophys. Res. - Atmos. **1993,** 98, 23207-23222.

20. Whalley, C. L.; Gómez Martín, J. C.; Wright, T. G.; Plane, J. M. C. A Kinetic Study of Mg^+ and Mg-containing Ions Reacting with O_3, O_2, N_2, CO_2, N_2O and H_2O: Implications for Magnesium Ion Chemistry in the Upper Atmosphere. Phys. Chem. Chem. Phys. **2011,** 13, 6352-6364.

21. Maitland, G. C. Intermolecular Forces : their Origin and Determination. Clarendon Press: Oxford, 1987.

22. Crank, J. The Mathematics of Diffusion. Oxford Science Publications: Oxford, 1986.

23. Lide, D. R. Handbook of Physics and Chemistry, 87th. edn. CRC Press: Boca Raton, FL, 2006.

24. Kokkin, D. L.; Dewberry, D.; Steimle, T. C. The Permanent Electric Dipole Moment of Nickel Oxide, NiO. Chem. Phys. Lett. **2014,** 609, 1-5.

25. De Avillez Pereira, R.; Baulch, D. L.; Pilling, M. J.; Robertson, S. H.; Zeng, G. Temperature and Pressure Dependence of the Multichannel Rate Coefficients for the CH_3+ OH System. J. Phys. Chem. **1997,** 101, 9681-9693.

26. Rollason, R. J.; Plane, J. M. C. The Reactions of FeO with O_3, H_2 , H_2O, O_2 and CO_2. Phys. Chem. Chem. Phys. **2000,** 2, 2335-2343.

27. Self, D. E.; Plane, J. M. C. A Kinetic Study of the Reactions of Iron Oxides and Hydroxides Relevant to the Chemistry of Iron in the Upper Mesosphere. Phys. Chem. Chem. Phys. **2003,** 5, 1407–1418.

28. Gilbert, R. G.; Smith, S. C. Theory of Unimolecular and Recombination Reactions. Blackwell: Oxford, 1990.

29. Smith, I. W. M. Kinetics and Dynamics of Elementary Gas Reactions. Butterworths: London, 1980.

30. Georgievskii, Y.; Klippenstein, S. J. Long-range Transition State Theory. J. Chem. Phys. **2005,** 122, art. no. 194103.

31. Kolb, C. E.; Worsnop, D. R.; Zahniser, M. S.; Robinson, G. N.; Shi, X.; Herschbach, D. R. Chemical Kinetics and Dynamics of the Mesospheric Sodium Nightglow. In Gas Phase Metal Reactions, Fontijn, A., Ed. Elsevier: Amsterdam, 1992; pp 15-27.

32. Plane, J. M. C.; Whalley, C. L. A New Model for Magnesium Chemistry in the Upper Atmosphere. J. Phys. Chem. A **2012,** 116, 6240–6252.

33. Smirnov, V. N. Rate Constant of the Gas-phase Reaction between Fe Atoms and CO_2. Kinet. Catal. **2008,** 49, 607-609.

34. Rollason, R. J.; Plane, J. M. C. A Kinetic Study of the Reactions of MgO with H_2O, CO_2 and O_2: Implications for Magnesium Chemistry in the Mesosphere. Phys. Chem. Chem. Phys. **2001,** 3, 4733-4740.

35. Gerding, M.; Alpers, M.; von Zahn, U.; Rollason, R. J.; Plane, J. M. C. Atmospheric Ca and Ca^+ layers: Midlatitude observations and modeling. Journal of Geophysical Research: Space Physics **2000,** 105, 27131-27146.

36. Helmer, M.; Plane, J. M. C. Kinetic Study of the Reaction between Fe and O_3 under Mesospheric Conditions. J. Chem. Soc., Faraday Trans. **1994,** 90, 31-37.

37. Marsh, D. R.; Mills, M. J.; Kinnison, D. E.; Lamarque, J.-F.; Calvo, N.; Polvani, L. M. Climate Change from 1850 to 2005 Simulated in CESM1(WACCM). J. Climate **2013,** 26, 7372-7391.

38. Helmer, M.; Plane, J. M. C. Experimental and Theoretical Study of the Reaction Fe + $O_2 + N_2 \rightarrow FeO_2 + N_2$. J. Chem. Soc., Faraday Trans. **1994,** 90, 395-401.

TOC graphic

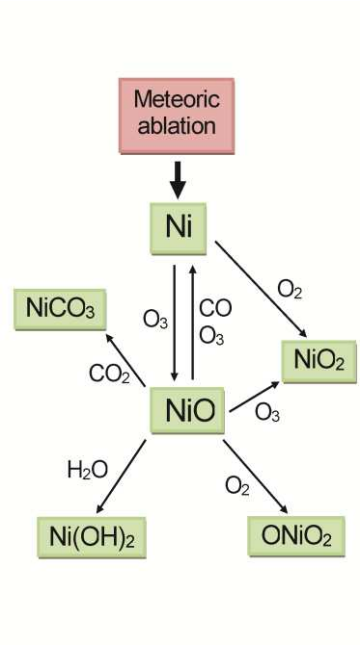
Meteoric ablation
Ni
O2
NiO2
NiCO3
O3
CO
O3
CO2
NiO
O3
H2O
O2
Ni(OH)2
ONiO2